Acta Cryst. (1983). A**39**, 315–321

Peak-Shape Analysis for Protein Neutron Crystallography with Position-Sensitive Detectors*

BY BENNO P. SCHOENBORN†

Biology Department, Brookhaven National Laboratory, Upton, Long Island, NY 11973, *USA*

(*Received* 1 *March* 1982; *accepted* 15 *December* 1982)

Abstract

In neutron protein crystallography, the use of position-sensitive detectors controlled by a modern data-acquisition system permits new approaches to data-collection strategies. Instead of dealing with conventional scans, like the θ–2θ scan, that provide an integrated intensity as a function of a rotational parameter, the computer-linked counter can be used to produce a three-dimensional reflection profile. As the crystal steps ($\Delta\omega$) through a reflection, the observed data for each step are stored in an external memory as a function of extent in 2θ and height (y) of a reflection. In this space, the reflection will be a three-dimensional distribution with dimensions determined by such basic geometrical conditions as $\Delta\lambda$, crystal size, mosaic spread, counter-resolution, and beam-collimation parameters. Knowledge of the interaction of these basic parameters will allow the design of optimal beam optics and will permit the delineation of the reflection from the background and permit, therefore, an accurate intensity determination.

Introduction

It has long been recognized that neutrons provide an excellent probe to use in analyzing the atomic and molecular structure of proteins (Schoenborn, 1969; Hanson & Schoenborn, 1981) and other large complexes like nerve membranes, retinal rods, ribosomes, viruses, chromatin, *etc.* (Schindler, Langer, Engelman & Moore, 1979; Jacrot, 1976). To improve the utilization of neutrons, position-sensitive detectors (Alberi, Fischer, Radeka, Rogers & Schoenborn, 1975) and efficient monochromators (Saxena & Schoenborn, 1977) have been developed to counter the effect of the relatively low thermal neutron flux available even at the most optimum high-flux beam reactors. The development of the position-sensitive ^{3}He counters with their limited resolution of ~3 mm and the development of multilayer monochromators with their inherent large but adjustable $\Delta\lambda$ have prompted this re-evaluation of data collection techniques. For biological specimens, which are often weak scatterers, the accurate integration of reflections is particularly important because of the large background produced by the significant incoherent scattering of hydrogen atoms.

Statistically accurate intensities are particularly important in neutron protein crystallographic investigations that attempt to localize H atoms and H/D exchange. This task involves the evaluation of approximately twice as many atoms as the equivalent X-ray analysis that determines only carbon-, nitrogen- and oxygen-atom locations.

The most efficient strategy for collecting three-dimensional neutron structure-factor data depends on the unit-cell size, the required resolution, the available detector, and the neutron flux. An understanding of the properties that cause particular peak shapes is needed for the precise integration of peaks and the design of efficient neutron spectrometer optics to maximize the diffraction intensity. The determination of the reflection shape presented in this paper is based on the normal beam geometry used in conjunction with linear or two-dimensional position-sensitive detectors. The spot shape is dependent on the order of the reflection (reciprocal-lattice spacing, *e.g.* $2\sin\theta/\lambda$), the beam divergence ε, the monochromator lattice spacing and resultant wavelength spread $\Delta\lambda$, the crystal size, crystal mosaic μ, and counter resolution. The use of two-dimensional detectors for X-ray protein crystallography has been described by others, notably by Xuong, Freer, Hamlin, Nielson & Vernon (1978). The X-ray case is simpler, the signal is larger, the background is smaller and spot smearing effects due to $\Delta\lambda$, counter resolutions and crystal size are negligible. In this paper the properties of the neutron case are considered.

A number of authors (Cooper & Nathans, 1968; Werner, 1971; Cagliotti & Ricci, 1962; Dachs, 1961; Willis, 1960) have described the resolution function arising from the neutron diffraction geometry in terms of Gaussian convolution for conventional ω or ω–2θ scans. In this paper, a numerical approach is presented

* Research carried out at Brookhaven National Laboratory under the auspices of the Department of Energy.

† Part of this paper was written while on sabbatical leave in the Department of Physics at the University of New South Wales and the Division of Chemical Physics at the CSIRO in Australia.

0567-7394/83/030315-07$01.50

to calculate the reflection shape as observed on a position-sensitive detector and to highlight individually the smearing effect of the different contributors, which may not always be Gaussian. Note that in the normal beam method selected, which is suitable for use with 2D counters, reflections are collected in layer lines.

The shape of a reflection

Fig. 1 depicts the schematic diagram of the experimental setup used. The high-flux beam reactor at BNL uses enriched uranium with D_2O moderation to produce a high flux of thermal neutrons with the maximum wavelength flux distribution peaking at ~1·1 Å. White radiation from the moderator region is collimated by the beam plug, monochromatized, and collimated again before hitting the crystal; no collimation exists between the crystal and the position-sensitive detector. The crystals are mounted in such a way that their most densely populated reciprocal-lattice planes are horizontal, to coincide with the high-resolution direction of the two-dimensional counter. The crystals are then rotated in small $\Delta\omega$ steps (~0·05°), the detector remaining stationary. For a given reflection, every ω step results in a 2θ–y profile, and reflections centered at $2\theta_{hkl}$ and ω_{hkl} are stored as three-dimensional arrays, as shown in Fig. 2. This three-dimensional array is summed along the vertical y direction to produce an ω–2θ projection, since changes in y are small and monotonic. For higher-layer lines the horizontal axis $2\theta'$ is the projection of 2θ. The use of a two-dimensional reflection representation simplifies the discussion somewhat and reduces the computational effort, which is particularly desirable for on-line calculations. The reflection within this array is approximately ellipsoidal and can be characterized by an inclination angle β and major and minor axes. The orientation and shape of such depicted reflections vary as a function of hkl. To obtain integrated intensities with an accurate subtraction of background the shape (extent) and orientation of the reflection have to be known. Usually, a reflection is integrated by adding all elements within a rectangular area that contains the peak and subtracting background scaled to the equivalent area.

The variance of the peak intensity is the sum of the total intensity (peak and background) within the integration area and the variance of the background scaled to the peak area. With n elements under the peak and m elements in the background, the scale is given by n^2/m^2. This variance is reduced if the variance of the scaled background is minimized with $m > n$ and the chosen peak area is no larger than the actual diffracted beam.

The analysis of reflection shapes described below allows the delineation of the peak shapes to minimize the area of integration and, therefore, reduces the statistical error of reflections. A further reduction in counting statistical error can be achieved by reducing the peak size itself by optimizing the diffraction conditions. The following analysis describes the magnitude of the reflection broadening effects of parameters like beam divergence, crystal mosaic, counter resolutions, monochromator spacing and wavelength bandwidth $\Delta\lambda$.

One method of finding peak shapes was proposed by Spencer & Kossiakoff (1980). This involves the use of a filtering technique to determine the reflection shape from the data. Sjolin & Wlodawer (1980) have further modified and used this procedure for the analysis of X-ray and neutron data. It should, however, be noted that the ellipsoid tilt angle, β, used in their approach depends strongly on $\Delta\lambda$ and the counter resolution. The

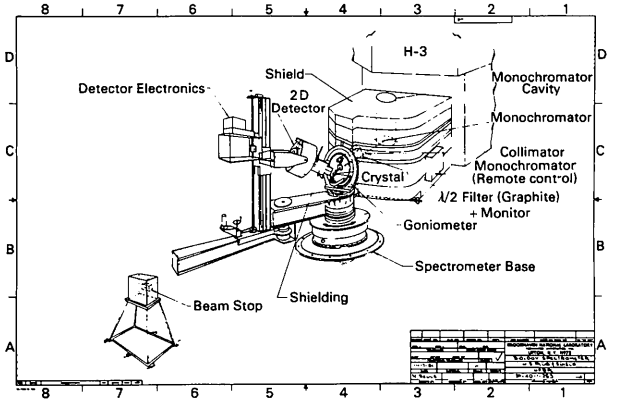

Fig. 1. Schematic drawing of the protein crystallography station at the BNL high-flux beam reactor (HFBR).

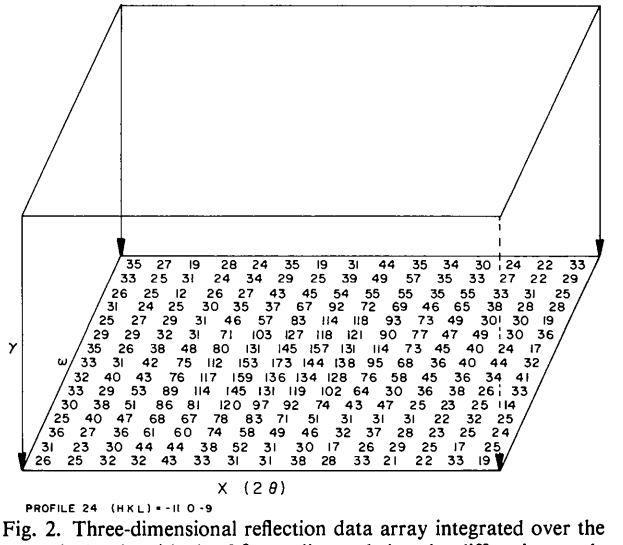

Fig. 2. Three-dimensional reflection data array integrated over the vertical axis with the 2θ coordinates being the diffraction angle coincident with the horizontal counter axis; ω = crystal rotation axis, perpendicular to the beam and parallel to the vertical axis. Unit step in ω and $2\theta = 0{\cdot}07°$.

orientation angle β described by Wonacott (1977) for X-ray data is therefore not applicable to neutron data. An alternative approach is presented here, based on the determination of the theoretical reflection shape from the basic diffraction condition applied for use with two-dimensional detectors.

(*a*) *The effect of beam divergence*

A finite beam diffracted from a monochromator with a mosaic μ will have a component that is purely monochromatic with a beam divergence ε. The effect of this component on the reflection profile is easily depicted in an Ewald-sphere construction. A divergent source beam will produce two boundary Ewald spheres of the same radius ($r = 1/\lambda$) inclined at an angle ε. A reflection with a given reciprocal-lattice vector ν will be in a diffraction position (Fig. 3) as it moves from A to B; the crystal rotates around an axis perpendicular to the plane of the drawing by angle $\Delta\omega$. From equal triangles, it is easily seen that $\Delta\omega = \varepsilon$ and, in an ω–2θ plot, the effect of beam divergence will produce an intensity distribution along a line oriented at an angle $\alpha = 45°$; this intensity distribution can usually be taken as a Gaussian, although, depending on the collimation used, it may have a trapezoidal shape.

(*b*) *The effect of crystal mosaic*

The effect of the crystal mosaic on the reflection profile is again easily described by a simple Ewald-sphere construction (Fig. 4). It is seen that, on rotation of the crystal, crystallites disordered by an angle μ produce a reflection during the rotation interval $\Delta\omega$, with $\Delta\omega = \mu$ being the width of the mosaic disorientation. In the ω–2θ graph, this produces intensity along the ω axis ($\alpha = 90°$) with an intensity distribution that is often Gaussian. For higher layer lines, the effective mosaic is still mainly observed as an intensity distribution as a function of ω, ($\alpha \sim 90°$) but is larger by the fraction ν/ν', where ν is the length of the reciprocal-lattice vector and ν' is the projection of that vector perpendicular to the rotation axis, *e.g.* $\nu' = (\nu^2 - \tau^2)^{1/2}$ where τ = reciprocal-layer-line height. In a monochromatic beam with divergence, the effect of the mosaic contribution occurs for every beam direction, *e.g.* the effect of the mosaic is applied to every point between A and B in Fig. 3. This produces a convolution (Lipson & Taylor, 1958) of the two intensity functions, with the effect of beam divergence localized at $\alpha = 45°$ and the mosaic effect at $\alpha = 90°$. For this example, both probability functions are taken to be Gaussian; in the numerical approach used any distribution can, however, be used.

For the beam divergence effect:

$$P(\omega) = \frac{1}{\sqrt{2\pi\varepsilon}} \exp\left[-\frac{1}{2}\left(\frac{\Delta\omega}{\varepsilon}\right)^2\right]$$

with $\Delta 2\theta = \Delta\omega$; and for the mosaic distribution:

$$P(\Delta\omega, \Delta 2\theta = 0) = \frac{1}{\sqrt{2\pi\mu}} \exp\left[-\frac{1}{2}\left(\frac{\Delta\omega}{\mu}\right)^2\right].$$

In practice, the probabilities are calculated for a range in ω in small steps ($\Delta\omega \sim 0{\cdot}05°$) to a cutoff limit where $P < 0{\cdot}001$. These two functions are then numerically convoluted to produce a two-dimensional (ω–2θ) probability density distribution. In general, contours of equal probability, $P_{\varepsilon,\mu}$ are ellipsoidal in shape with the major axis inclined at an angle between 45 and 90° (Fig. 5*a*), depending on the relative magnitudes of ε and μ.

(*c*) *The effect of crystal size*

The finite width of a crystal results in the superposition of the probability ellipse $P_{\varepsilon,\mu}$ at every point of the effective crystal width. In practice, for the ω–2θ representation, this results in a convolution of $P_{\varepsilon,\mu}$ with a square wave in the $\Delta 2\theta$ direction. The resultant convolution P_τ is shown in Fig. 5(*b*) for a crystal width

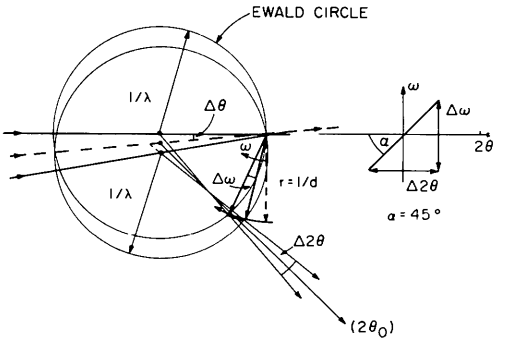

Fig. 3. Ewald-sphere construction describing the effect of beam divergence for a given λ on the diffraction process. The reciprocal-lattice vector $\nu = 1/d$ is in diffraction condition for the rotational width $\Delta\omega$ (heavy line) producing diffraction over the angular width $\Delta 2\theta$ centered on the Bragg angle $2\theta_0$. On the right, the resulting intensity distribution (heavy line) is mapped as a function of the crystal rotation ω and the diffraction angle 2θ.

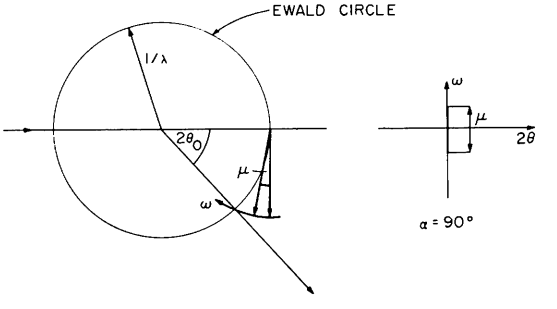

Fig. 4. Ewald-sphere construction describing the effect of the crystal mosaic for a given wavelength λ. The reciprocal-lattice vectors ν distributed within angular width μ produce diffraction at the Bragg angle $2\theta_0$ over the rotational width $\Delta\omega = \mu$.

of 2 mm. If the crystal is very asymmetric, the effective width of this function will vary with the crystal rotation ω.

(d) The effect of counter resolution

Position-sensitive detectors with their limited resolution produce further reflection smearing. Most of the currently existing position-sensitive detectors have resolutions of 3 to 10 mm, and only recently, with the development of a new readout system, has it become possible to produce position-sensitive detectors with resolutions less than 2 mm. The detector smearing along the vertical axis is of no concern here, since data represented in the ω–2θ space have been integrated along that direction. Along the horizontal direction parallel to the 2θ axis, the limited resolution of the detector gives rise to a detector smearing which is Gaussian and broadens the peak in the $\Delta 2\theta$ direction.

$$P_D(\Delta\omega = 0, \Delta 2\theta) = \frac{1}{\sqrt{2\pi}\delta} \exp\left[-\frac{1}{2}\left(\frac{2\theta}{\delta}\right)^2\right].$$

This probability distribution is again evaluated numerically and is then convoluted with the probability distribution $P_\tau(\Delta\omega, \Delta 2\theta)$. The resultant distribution is shown in Fig. 5(*c*). This large spot smearing would significantly increase reflection overlap if the conventional 2θ integration scheme were used. The profile broadening due to the crystal size and that due to the limited detector resolution can in many cases be treated as one effect. Proper integration of reflections in the ω–2θ space minimizes such overlap, requiring, however, storage of each diffraction profile as a function of ω and 2θ.

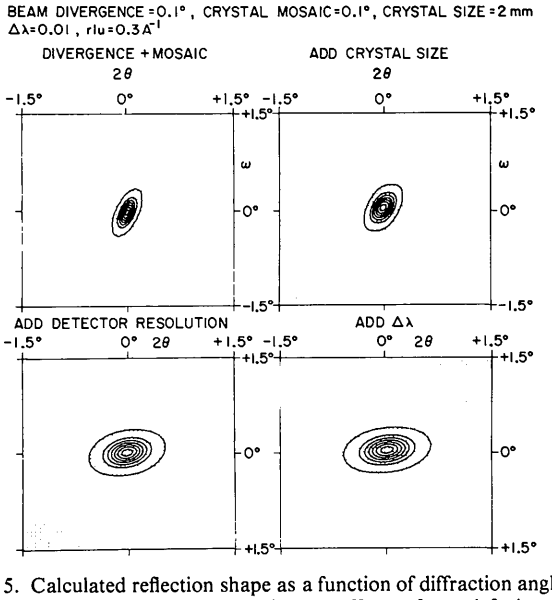

Fig. 5. Calculated reflection shape as a function of diffraction angle 2θ and crystal rotation ω showing the effects of: top left: beam divergence and crystal mosaicity; top right: the added effect of the crystal size (2 mm); lower left: the added effect of the detector resolution (3 mm); lower right: the effect of the wavelength bandwidth $\Delta\lambda$.

(e) The effect of $\Delta\lambda$

The above considerations apply more or less directly to the X-ray case, although the resolution for X-ray position-sensitive detectors is much better (~0·3 mm). Proper integration of the reflection in the ω–2θ space should give intensities which are physically more realistic. The X-ray case has been described by Mathieson (1982) for single-crystal diffractometry without a monochromator. In the neutron case, the effect of $\Delta\lambda$ has to be considered, since the wavelength bandwidth $\Delta\lambda$ is large and is often deliberately increased to improve flux.

The neutron source has a finite size and produces radiation with a divergence ε determined by the collimation; this beam divergence and the mosaic of the monochromator result in a diffracted beam with a given wavelength bandwidth $\Delta\lambda$. $\Delta\lambda$ is calculated from the differentiated Bragg equation and $\Delta\lambda = \lambda\Delta\theta \cot\theta_M$, where $\Delta\theta = \varepsilon$ is the beam divergence and θ_M is the Bragg angle of the monochromator. With the monochromator set for a wavelength λ with a Bragg angle θ_M, the extreme path of the neutrons in the horizontal plane are then at angles $\theta_M + \Delta\theta$ and $\theta_M - \Delta\theta$. These extreme rays correspond, therefore, to wavelength $\lambda_{min} = \lambda(1 - \Delta\theta \cot\theta_M)$ and $\lambda_{max} = \lambda(1 + \Delta\theta \cot\theta_M)$. The monochromator, therefore, sorts out the wavelength according to angle with the longer wavelength emerging at higher angles. The effect of $\Delta\lambda$ on the diffraction condition is again depicted by an Ewald-sphere construction (Fig. 6). In this case, the two limiting spheres have radii $r_1 = 1/(\lambda - \Delta\lambda)$ and $r_3 = 1/(\lambda + \Delta\lambda)$. The equatorial circles will intersect at two points, the origin of the reciprocal lattice at 0 and the point M, the so-called focusing position at the end of the reciprocal-lattice vector ν_m of the monochromator spacing (Arndt & Willis, 1966). In this construction, the required diffraction conditions are satisfied for all points in the shaded area. A reciprocal-lattice vector ν rotating perpendicular to the rotation axis ω located at 0 will produce diffraction from point P_1 to P_3; during the rotation $\Delta\omega$, the resulting rays will diverge at an angle $\Delta 2\theta$.

The polychromaticity of the beam results, therefore, in the spreading of the intensity of an ideal reflection along a line of length l inclined at an angle α. The magnitude of the length l and the angle depend on the reciprocal-vector length (*e.g. hkl*) and the basic diffraction condition. This diffraction behavior is again best depicted in the ω–2θ space (Fig. 6) with a reflection of length l inclined at an angle α. The vector ν crosses the circle r_1 and r_3 at rotation angles ω_1 and ω_3.

Note that the origins of the Ewald circles are not concentric. Therefore, in a numerical approach, the vector v is rotated along ω, and the distances (d) from the end of vector v to the respective Ewald centers (C_1 or C_3) are calculated. Intercepts occur when $d_1 = v_1$ and $d_3 = v_3$. The origin of the coordinate system is at C_2, the center of the Ewald sphere for the average value of λ.

For given intercepts P_1 and P_3, the respective diffraction angles ($2\theta_1$ and $2\theta_3$) are calculated. Scattering angles are measured with respect to the origin of the mean Ewald sphere. While rotating ω, a reflection will be observed moving from $2\theta_3$ to $2\theta_1$ as depicted on the right side of Fig. 6. The reflection center occurs at the Bragg angle for the mean wavelength. In Fig. 7, the reflection length and orientation due to the effects of $\Delta\lambda$ only are presented as a function of reciprocal length v. The data in Fig. 7(a) are from calculations performed for a graphite monochromator set at $\theta_M = 13°$ for a wavelength of 1·5 Å and a beam divergence of 0·04° with $\Delta\lambda = 0{\cdot}005$ Å. Fig. 7(b) shows the same data but for a multilayer monochromator used for small-angle diffraction with $\lambda = 5{\cdot}4$ Å, $\theta_M = 2{\cdot}1°$, and a beam divergence of 0·1° with a resulting $\Delta\lambda$ of 0·26 Å.

Inspection of Fig. 6 shows that special conditions arise for $v = v_M$ and $v = 0{\cdot}5v_M$:

$$\text{at } v = 0{\cdot}5v_M,\ \Delta 2\theta = 0° \text{ and } \alpha = -90°;$$

$$\text{at } v = v_M,\quad \Delta\omega = 0° \text{ and } \alpha = 0°.$$

The intensity distribution $P_{\Delta\lambda}$ due to $\Delta\lambda$ is assumed to be Gaussian. Since this intensity distribution reflects only the effect of $\Delta\lambda$, the effects due to (a) beam divergence, (b) crystal mosaic, (c) crystal size, and (d) counter resolution have to be applied to every point over the reflection length l. Note that the beam divergence ε affects the reflection smearing twice: (1) as discussed in § (a) where the effect of beam divergence for a given wavelength λ is discussed; and (2) the effect of beam divergence on the magnitude of the wavelength bandwidth $\Delta\lambda$. In practice, this convolution is again performed numerically in the conventional way by multiplying P with $P_{\Delta\lambda}$ for every point over the length l and then adding all the respective contributions to produce the final intensity distribution $P_R(\omega_1 \Delta 2\theta)$; $\Delta\omega = 0$ and $\Delta 2\theta = 0$ are the conditions for the mean Bragg peak. Fig. 5 shows the effect of the successive convolutions while Fig. 8 depicts the spot-shape variation as a function of reciprocal-lattice length $v = 2 \sin\theta/\lambda$.

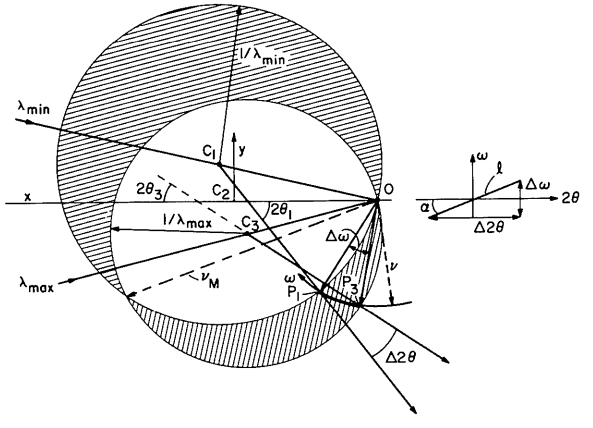

Fig. 6. Ewald-sphere construction showing the width of a reflection due to $\Delta\lambda$, the wavelength bandwidth. The limiting spheres for the smallest (λ_{min}) and the largest wavelength (λ_{max}) are drawn. Diffraction occurs at any point in the shaded regions. The large shaded region at the top is due to diffraction in the 'antiparallel' mode (Arndt & Willis, 1966). The shaded region on the bottom represents diffraction in the parallel or focusing mode. The vector length ν_M is given by the lattice spacing of the monochromator selecting the radiation. On rotation, the reciprocal-lattice vector ν (of the sample) will be in reflecting position from P_1 to P_3 over the rotational width $\Delta\omega$ and will produce diffraction over an angle $\Delta 2\theta$. $\Delta\omega$ and $\Delta 2\theta$ vary as a function of reciprocal-lattice length ν and layer-line height τ (τ is perpendicular to the plane of the drawing). The diffraction process is mapped on the right side as a representative function of ω and 2θ. α is the angle formed between the diffraction line and the horizontal axis (2θ). The reflection length l is the length of the distribution at half-height measured in degrees.

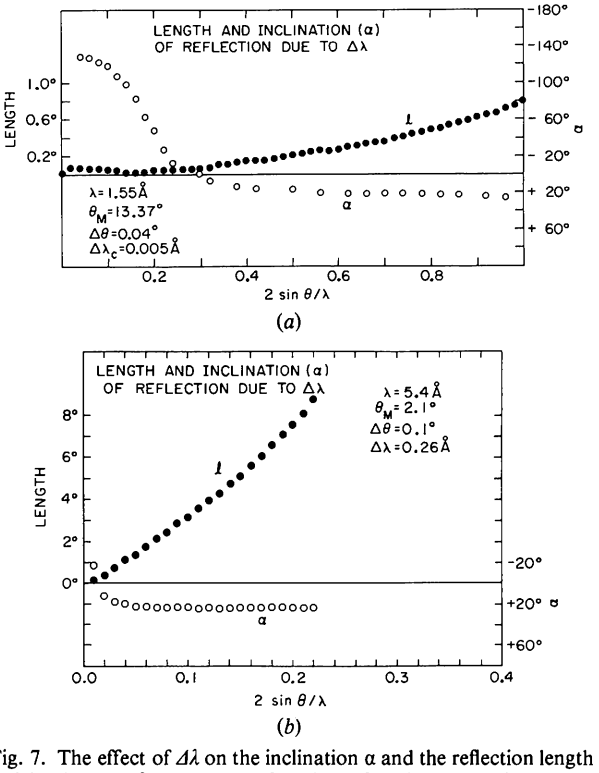

Fig. 7. The effect of $\Delta\lambda$ on the inclination α and the reflection length l in the ω–2θ space as a function of reciprocal-lattice length $v = 2 \sin\theta/\lambda$ (see Fig. 6). (a) For a graphite monochromator with $\theta_M = 13{\cdot}4°$. (b) For a multilayer monochromator with $\theta_M = 2{\cdot}1°$.

Table 1. *Observed and calculated spot-shape parameters for some well characterized test crystals*

The axes lengths are calculated from the second moments of the distribution and are equivalent to the half-width at half-height. For data delineation purposes the full half-length of the axes are determined to include 99·9% of the intensity. These lengths are ~3 times the length at half-height. For the alumina and germanium data the final grid size is 0·16° in $\Delta\omega$ and $\Delta 2\theta$, for KBr $\Delta\omega = \Delta 2\theta = 0{\cdot}08°$. These grid intervals are determined by the final array size of 100 × 100 elements that encloses the full reflection.

Crystal	Monochromator setting (°)	Beam divergence (°)	Crystal mosaic (°)	λ (Å)	ν (Å^{-1})	Angle α Calc. ±3°	Angle α Obs. ±3°	Major-axis length Calc. ±0·30°	Major-axis length Obs. ±0·30°	Minor-axis length Calc. ±0·1°	Minor-axis length Obs. ±0·1°
Alumina	2·1*	0·2	0·1	5·4	0·08	28	25	1·3	1·2	0·1	0·1
KBr	13·4†	0·05	0·15	1·5	0·35	2	0	0·5	0·6	0·3	0·4
					0·71	7	5	0·8	0·8	0·3	0·4
Germanium	13·4†	0·08	0·001	1·5	0·30	6	4	1·0	0·9	0·3	0·2
					0·50	8	9	1·4	1·8	0·4	0·5
					0·59	16	12	1·8	1·5	0·3	0·3

* As in Fig. 7(*b*) for a multilayer monochromator.
† As in Fig. 7(*a*) for a graphite monochromator.

To delineate the shape of the reflection for accurate integration, the spot shape is described by minor and major ellipsoidal axes with the major axis inclined by an angle β towards the $\Delta 2\theta$ coordinate axis (Table 1). These parameters are best calculated from the second moments of the calculated intensity distribution as derived by Lambe (1958).

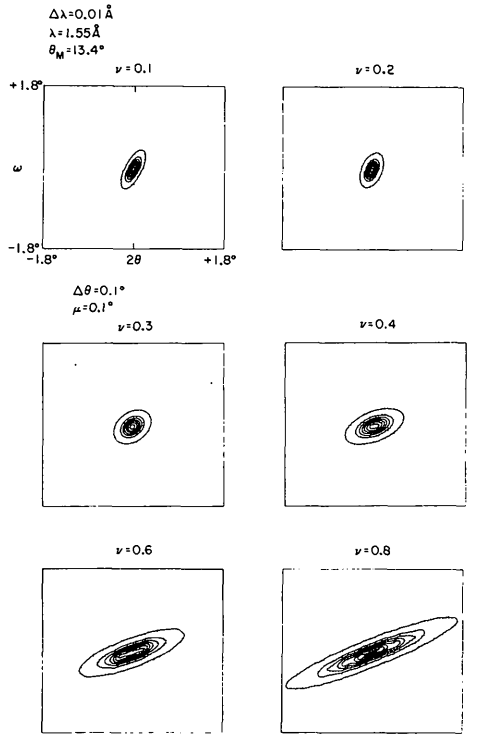

Fig. 8. The combined effect of crystal mosaicity, beam divergence and $\Delta\lambda$ on the shape of reflections as a function of reciprocal Bragg spacing, $\nu = 2 \sin\theta/\lambda$. Sampling of the reflection profile at given intervals produces the ripple effect for plots with the larger reciprocal spacings. Note that crystal size and counter resolution effects have not been applied in this case.

Comparison of calculated spot shape with experimental data

In neutron crystallography the background from a hydrogen-containing protein crystal is very high compared with coherent diffraction intensities. While the number of very strong reflections is small, there are many that can be used to check the validity of the spot-shape calculation described above. To compare reflection shapes, the inclination angles β and the axial widths are determined and compared to observed reflections. For proteins, no strong reflections are, however, observed at higher angles, and data from a perfect germanium and other crystals were used to check this approach (Table 1). These tests show that the described spot-shape calculation agrees well with experimental data, and shape parameters are accurate in most cases to within the spacing of one array element. These shape parameters can then be used to define the area of integration to the actual extent of a reflection, minimizing the variance of the peak integration and also reducing reflection overlap. The way the diffraction conditions interact to produce the observed spot shapes is easily discerned from Figs. 5 and 8. These drawings show that $\Delta\lambda$ and counter resolution account for most of the peak broadening in the presently used setup. The effect of changes in beam geometry on peak shapes can directly be tested by the described procedure. It is thus possible to optimize diffraction conditions for high flux and good peak-to-background ratios.

Data collection and processing strategy

The crystal is mounted so that reciprocal-lattice planes with the highest reflection density lie in the equatorial plane, which is also the direction having the highest counter resolutions (Cain, Norvell & Schoenborn, 1975). The crystal is then rotated in discrete steps (~0·05°) through ω, which is the axis perpendicular to

the beam. The ω–2θ coordinates of reflections *hkl* are calculated from the crystal orientation matrix for reflections that fall on the detector. The unit-cell dimensions and the detector characteristics determine the spatial resolution and fix the crystal-to-detector distance, which for a medium-size protein is typically 60 to 100 cm. With a detection area of 20 × 20 cm an acceptance angle of ~18° is possible, permitting observations of many simultaneous reflections, depending on the overall 2θ and λ settings. For the duration of every ω step (~60 s), the whole counter is mapped into a direct addressable external memory. At the end of every step and for every active reflection, a counter region Δy (height) and $\Delta 2\theta$ is extracted and is stored separately as a function of ω. A reflection is represented, therefore, as a three-dimensional data array centered on $2\theta_{hkl}, y_{hkl}, \omega_{hkl}$. This array is also stored on disk for further processing, as described below.

The best peak-to-background ratio is achieved by delineating the reflection as a three-dimensional ellipsoid. In practice, however, this is very time consuming for on-line integration. The reflection is, therefore, summed over Δy to produce a two-dimensional profile in ω–2θ, which is then integrated after delineation of the reflection according to precalculated spot-shape parameters as described above. The height Δy of reflections can be determined from similar calculations but is best estimated from the observed size of a few strong reflections since changes in Δy are small and monotonic.

For strong reflections the center of mass is determined after background subtraction to monitor the crystal alignment and the counter electronics. Note that the position readout of a well-adjusted counter is, however, linear and stable over many months, with a positional reproducibility better than 0·5%. The orientation of strong reflection within this ω–2θ array is then determined to check on the precalculated orientation parameters. The observed as well as the precalculated spot-shape parameters are stored as a function of $2 \sin \theta/\lambda$ and layer-line height (τ).

Areas outside of the delineated reflections are used as background. The background information may be accumulated for given regions of reciprocal-lattice volume to improve the counting statistics. Background is, therefore, averaged for a number of reflections (~100). Reflections with backgrounds showing large deviations from their group average are eliminated and marked. Since reflections collected at the beginning suffer from lack of background accumulation, a second cycle of integration is beneficial using the accumulated background from the whole data set. The integration of reflections as described above minimizes the area of peak integration and, compared to the usual channel summation technique, reduced the statistical error (σ) by $\frac{1}{3}$ for a myoglobin data set (Schoenborn, 1983). Usage of the described background table further reduces the σ of reflections by $\frac{1}{3}$.

The author wishes to thank Dr A. McL. Mathieson for many discussions and for communicating his results prior to publication. The author wishes to thank Dr D. Schneider for a critical review of this paper and Mary Rustad for help in the preparation of the manuscript.

References

ALBERI, J., FISHER, J., RADEKA, V., ROGERS, L. C. & SCHOENBORN, B. P. (1975). *IEEE Trans. Nucl. Sci.* NS-**22**, 255–266.

ARNDT, U. W. & WILLIS, B. T. M. (1966). In *Single Crystal Diffractometry*. Cambridge Univ. Press.

CAGLIOTTI, C. & RICCI, F. P. (1962). *Nucl. Instrum. Methods*, **15**, 155.

CAIN, J. E., NORVELL, J. C. & SCHOENBORN, B. P. (1975). *Brookhaven Symp. Biol.* **8**, 43–50.

COOPER, M. J. & NATHANS, R. (1968). *Acta Cryst.* A**24**, 619–624.

DACHS, H. (1961). *Z. Kristallogr.* **115**, 80–92.

HANSON, J. C. & SCHOENBORN, B. P. (1981). *J. Mol. Biol.* **153**, 117–146.

JACROT, B. (1976). *Rep. Progr. Phys.* **39**, 911–953.

LAMBE, C. G. (1958). In *Applied Mathematics for Engineers*. London: The English Univ. Press.

LIPSON, H. & TAYLOR, C. A. (1958). In *Fourier Transforms and X-ray Diffraction*. London: Bell.

MATHIESON, A. McL. (1982). *Acta Cryst.* A**38**, 378–387.

SAXENA, A. M. & SCHOENBORN, B. P. (1977). *Acta Cryst.* A**33**, 805–813.

SCHINDLER, D. G., LANGER, J. A., ENGELMAN, D. M. & MOORE, P. B. (1979). *J. Mol. Biol.* **134**, 595–620.

SCHOENBORN, B. P. (1969). *Nature (London)*, **224**, 143–147.

SCHOENBORN, B. P. (1983). *Neutrons in Biology*, edited by B. P. SCHOENBORN. *Brookhaven Biol. Symp.* No. 32. In the press.

SJOLIN, L. & WLODAWER, A. (1980). *Acta Cryst.* A**37**, 594–604.

SPENCER, S. A. & KOSSIAKOFF, A. A. (1980). *J. Appl. Cryst.* **13**, 563–571.

WERNER, S. A. (1971). *Acta Cryst.* A**27**, 665–683.

WILLIS, B. T. M. (1960). *Acta Cryst.* **13**, 763–766.

WONACOTT, A. J. (1977). In *The Rotation Method*, edited by U. W. ARNDT & A. J. WONACOTT. Amsterdam: North Holland.

XUONG, N. H., FREER, S. T., HAMLIN, R., NIELSEN, C. & VERNON, W. (1978). *Acta Cryst.* A**34**, 289–296.